Journal of Colloid and Interface Science 599 (2021) 752–761

Contents lists available at ScienceDirect

Journal of Colloid and Interface Science

journal homepage: www.elsevier.com/locate/jcis

Regular Article

An electrochemical biosensor based on hemin/G-quadruplex DNAzyme and PdRu/Pt heterostructures as signal amplifier for circulating tumor cells detection

Xi Zhou [a], Qinli Pu [a], Hongyan Yu [a], Yang Peng [b], Junjie Li [a], Yujun Yang [a], Huajian Chen [a,c], Yaguang Weng [a,*], Guoming Xie [a,*]

[a] Key Laboratory of Clinical Laboratory Diagnostics (Chinese Ministry of Education), College of Laboratory Medicine, Chongqing Medical Laboratory Microfluidics and SPRi Engineering Research Center, Chongqing Medical University, No. 1 Yi Xue Yuan Road, Chongqing 400016, PR China
[b] Clinical Laboratory Medicine Center, Chongqing University Cancer Hospital, Chongqing 400030, PR China
[c] Chongqing Emergency Medical Center, Chongqing University Central Hospital, School of Medicine, Chongqing University, Chongqing, China

HIGHLIGHTS

- 3D hyperbranched PdRu/Pt heterostructures with excellent catalytic activity was synthesized to improve signal amplification.
- PdRu/Pt integrated with hemin/G-quadruplex DNAzyme was first utilized as signal probe.
- As-proposed biosensor reached a detection limit down to 2 cells mL^{-1}.

GRAPHICAL ABSTRACT

An enzyme-free sandwich-type electrochemical biosensor was developed for highly sensitive detection of CTCs by fabricating a novel PdRu/Pt hierarchical structures through a facile hydrothermal method and coupling with hemin/G-quadruplex as signal amplification probes. Meanwhile, high conductive Super P and gold nanoparticles (AuNPs) acted as sensing medium to improve electrical conductivity and immobilization of anti-EpCAM antibody to specifically capture model CTCs.

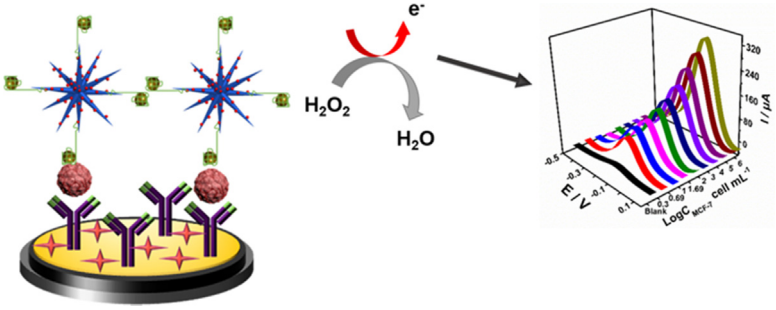

ARTICLE INFO

Article history:
Received 1 April 2021
Revised 29 April 2021
Accepted 1 May 2021
Available online 5 May 2021

Keywords:
PdRu/Pt heterostructures
Super P/gold nanoparticles
Hemin/G-quadruplex
Electrochemical biosensor
Circulating tumor cells

ABSTRACT

Metastasis due to circulating tumor cells (CTCs) shed from the original tumor accounts for the majority of cancer-related death. Efficient CTCs detection is pivotal to the diagnosis of early cancer metastasis. In this work, Platinum nanoparticles (PtNPs) decorated hyperbranched PdRu nanospines (PdRu/Pt) hierarchical structures were firstly synthesized to detect CTCs with the assistance of DNAzyme. Meanwhile, Super P and gold nanoparticles (AuNPs) acted as sensing medium to improve electrical conductivity and immobilization of anti-EpCAM antibody to specifically capture model CTCs. After immune-conjugation of anti-EpCAM-MCF-7-signal probes on the gold electrode, PtNPs, PdRu nanospines (PdRuNSs) and hemin/G-quadruplex co-catalyzed substrate H_2O_2 to realize multiplexed signal amplification, which significantly improves the analytical performance of the electrochemical biosensor. As-proposed biosensor reached a limit of detection (LOD) down to 2 cells mL^{-1} and showed a wide detection range of 2 to 10^6 cells mL^{-1}. Application of the biosensor to detect MCF-7 cells spiked human blood samples further demonstrated the feasibility for early cancer evaluation in clinic.

* Corresponding authors.
E-mail addresses: yaguangweng@cqmu.edu.cn (Y. Weng), guomingxie@cqmu.edu.cn, xiegm059@foxmail.com (G. Xie).

https://doi.org/10.1016/j.jcis.2021.05.006
0021-9797/

1. Introduction

CTCs are malignant cancer cells, which seldom secret from the original or metastasis tumor and discharge into bloodstream circulation [1]. Owing to the metastasis of cells in cancer progression at early stage, CTCs have emerged as an important biomarker for cancer monitor and diagnosis [2,3]. Compared with conventional imaging methods and pathological cytological techniques for routine tumor test, CTCs detection in peripheral blood is rendered to be convenient and non-invasive, and more importantly, would provide more information pertinent to metastasis monitoring, anticancer treatment and prognostic prediction [4].

Since the concentration of CTCs in peripheral blood is extremely low (usually lower than 10 cells per 10^6 to 10^8 mononuclear cells), accurate capture and detection of CTCs in real samples remains a big challenge [5]. Accordingly, immunoreaction-based methods for CTCs measurement have been developed, which include CellSearch platform, magnetic-activated cell sorting system (MACS) and subtraction enrichment and immunostaining fluorescence hybridization (SE-iFISH) [6–8]. These methods mainly rely on immunological recognition to separate and enumerate CTCs, and have shown high specificity and sensitivity. Recently, microfluidic devices that depend on physical properties like cell surface roughness, particle size, or density have also been reported to identify CTCs instead of surface markers [9]. Although these technologies have advanced the detection of CTCs to a larger extent, drawbacks such as complicate and time-consuming operation procedure and high equipment production costs greatly limited their application in clinical diagnosis. Therefore, it is an urgent need to explore more reliable and cost-effective method for the detection of rare CTCs.

Due to merits like cost-effectiveness and fast-responsiveness, electrochemical biosensors have demonstrated their advantages in a variety of fields [10,11]. To improve the analytical performance, integration of advanced materials capable of signal amplification has been extensively explored in electrochemical biosensors construction [12–14]. Specifically, Palladium (Pd), ruthenium (Ru) and Platinum (Pt) metals have been widely applied due to excellent electrocatalytic performance [15,16]. Additionally, reasonable structure design will not only improve utilization rate of metal precursor but also promote signal amplification effect after incorporation on electrode surface [17]. Apart from nanomaterials, DNA aptamers, which are functional oligonucleotide sequences, have also emerged as useful electrode decoration component in biosensor design [18]. AS1411, an aptamer toward nucleolin in tumor cell, can form G-quadruplex (G4) structure by Hoogsteen hydrogen bonds [19]. Due to merits of rapid synthesis, small size and being easy for labeling, hemin is selected and inserted into the G4 structure to form hemin/G-quadruplex (hemin/G4) DNAzyme, which displays as horseradish peroxidase (HRP)-mimicking to decompose inherent H_2O_2 to increase the sensitivity of the biosensor [20].

As an extension of the work in our group [21,22], Super P and AuNPs were combined herein to enhance electrical conductivity and sensitivity for electrochemical detection of CTCs. Super P exhibits excellent conductivity and could promote signal output after modification on gold electrode [23]. In addition, PtNPs decorated hyperbranched PdRu nanospines (PdRu/Pt) heterogeneous structures were synthesized for the first time to improve electrochemical response. Compared with PdRuPt alloy [24], PdRu/Pt heterostructures exhibited higher reactivity and excellent catalytic activity. Besides, we integrated hemin/G4 with PdRu/Pt to assemble the signal amplifying probe (SP). The SP can recognize the target cell with good specificity and further enhance the catalytic effect to amplify the signal responses simultaneously. To the best of our knowledge, this is the first report on the synthesis of PdRu/Pt for electrochemical biosensors construction. Amino-terminated AS1411, as recognition probe (RP), was attached onto the PdRu/Pt surface via Pt-NH_2 bond. Abundant hemin/G4 mimicking DNAzymes were formed after introduction of hemin to fabricated SP, further improving the sensitivity of the biosensor. With immobilized AuNPs and Super P to increase electrical conductivity and install anti-EpCAM antibody on electrodes, significant enhancement of electrical signal was recorded after model MCF-7 cell captured. We envision that this new enzyme-free sandwich-type electrochemical biosensor would advance early metastasis monitoring and clinical evaluation of tumors.

2. Experimental

2.1. Chemicals and apparatus

More information about the Chemicals and Apparatus was provided in Supporting information (SI).

2.2. Preparation of Super P and AuNPs

Firstly, 2.0 mg Super P was dispersed into 2.0 mL of 0.5 wt% chitosan solution with the favor of ultrasonic blending for 4 h to assess homogeneous mixed liquor. AuNPs were prepared by a classical citrate reduction method with slight modification [25]. Briefly, 50 mL of 0.01% (w/v) $HAuCl_4$ was stirring and boiling duration for 15 min, then chloroauric acid was oxidized by adding freshly-prepared 2% of 0.5 mL trisodium citrate aqueous solution dropwise. The mixture solution was stirred and boiled constantly for another 15 min until the color changed to bright wine red. Finally, AuNPs were collected by centrifugation, washing process and stored at 4 °C for future use after cooling to room temperature (RT).

2.3. Synthesis of the PdRuNSs

Herein, PdRuNSs were synthesized by a slow reduction at constant temperature. Typically, 3.25 mL of 30 mg F127 and 200 mg KBr were dissolved under sonication in aqueous solution and introduced into a sample vial, followed by homogeneously mixing with 20 mM $RuCl_3$ (0.375 mL) and 20 mM H_2PdCl_4 (1.125 mL). After that, 0.1 M freshly-prepared ascorbic acid solution (2 mL) was injected quickly into the aforementioned mixed solution. Subsequently, the reaction solution was kept in a water bath for 12 h at 70 °C, then the light reddish brown solution turned to black (Fig. S1). The products were cooling to RT for storage and analysis.

Additionally, Pd nanocrystals (PdNCs) were prepared by similar method, excepted 20 mM $RuCl_3$ (0.375 mL) precursor was replaced by deionized H_2O (0.375 mL).

2.4. Synthesis of hyperbranched PdRu/Pt heterostructures

This method was developed in our laboratory. Briefly, 5 mL of deionized water was added to 5 mL of the PdRuNSs solution presynthesized to stir mixture thoroughly and heat to 95 °C. Then, 0.5 mL of 1% H_2PtCl_6 was added. Afterwards, 0.4 mL of 40 mM AA was continuous dropped into the mixture, the reaction solution was stirred for another 20 min in constant 95 °C to form hyperbranched PdRu/Pt heterostructures. Finally, the black solid was collected by centrifugation at 8000 rpm for 10 min and washed three times with deionized water and ethanol, re-suspended with 3 mL purified water to obtain the PdRu/Pt homogenous solution. The solution was stored at 4 °C for subsequent usage.

2.5. Preparation of the hemin/G4 labelled PdRu/Pt (SP)

Immobilization of the RP onto the surface of PdRu/Pt was completed as state in following steps (Scheme. 1A). Firstly, 400 μL of prepared PdRu/Pt solution was mixed with 100 μL of RP (100 nM) followed by mild stirring at 37 °C for 12 h. Thus, RP was connected onto the PdRu/Pt nanomaterial surface through Pt-NH_2 bond. Then, 200 μL of hemin (0.5 mg/mL) was added into the mixture and stirred at 37 °C for 2 h to form the hemin/G4 structure. Finally, 0.5% BSA was introduced to block the inactive binding sites. The final product was centrifuged, resuspended in 400 μL of 0.01 M PBS and stored in 4 °C for further use.

Moreover, PdRuNSs-RP-BSA and PdRu/Pt-RP-BSA were prepared by the similar method, without adding 200 μL of hemin (0.05 mg/mL).

2.6. Fabrication of the biosensor

Scheme 1B exhibits the construction procedures of the sandwich-like biosensor. A gold electrode (3 mm in diameter) was polished beforehand with a 0.3 and 0.05 μm alumina slurry to a mirror-like finish, then the electrode was sonicated with absolute Milli-Q water, ethanol and Milli-Q water for 10 min in an ultrasonic bath in order to remove the remaining absorbed particles. Thus, a smooth interface was obtained. After the electrode was dried at room temperature, the electrode was activated in a fresh piranha solution (30% H_2O_2:98% H_2SO_4, 1:3 by volume) for 10 min, thoroughly rinsed with ultrapure water, and then dried in air. 8 μL of Super P suspension was dropped on the bare electrode and dried at RT, following 8 μL AuNPs was added and dried at 37 °C for 3 h. Then, eight microliters of the anti-EpCAM (70 μg mL^{-1}) in PBS (0.01 M, pH 7.4) was directly attached onto the modified electrode by incubation for 1 h at 37 °C with Au-NH_2 bonds. After rinsing with PBS (0.01 M, pH 7.4), the gold electrode was incubated with 0.4% BSA for 50 min at RT to block the unbound sites. Finally, the designed electrochemical biosensor was attained after washing with PBS and stored at 4 °C for further use.

2.7. Experiment on the specific binding ability of the aptamers and MCF-7 cells

In order to explore the ability to recognize and bind with specificity of MCF-7 cells and AS1411, HEK 293T cells were selected as negative control. MCF-7 cells and 293T cells were both cultured in a 24-well plate cell climbing film, incubated for 24 h at 37 °C. Then, the cells were washed with cold PBS for 2 times, 3 min for each time, followed by fixing with 10% formaldehyde for 30 min. After washing with cold PBS for 3 times, 500 μL of 2% BSA was adopted to block the active vacancies in cell plate. Next, FAM modified recognition probes (FAM-RPs) were added in each well plate and incubation for 60 min and washed with cold PBS. At last, the cells nuclei were stained with DAPI for 15 min protecting from light at room temperature, washed with cold PBS and took the photographs by using a fluorescence microscope.

2.8. Electrochemical measurement

Electrochemical measurements were executed with a CHI 660E electrochemical workstation in a three-electrode pattern, comprising an Au electrode as working electrode, a saturated KCl impregnated Ag/AgCl as reference electrode, and a Pt wire as auxiliary electrode. The designed electrochemical biosensor was measured by differential pulse voltammetry (DPV) from −0.6 V to 0 V with the voltage amplitude of 0.05 V in a pH 6.0 PBS (100 mM, 25 mL) containing 20 mM H_2O_2. Cyclic voltammetry (from −0.2–0.6 V) and electrochemical impedance spectroscopy (frequency sweep range: 100 kHz to 1 Hz; alternating voltage: 5 mV) were performed in 0.1 M KCl containing 5 mM $Fe(CN)_6^{3-/4-}$, respectively, for characterization of the electrochemical biosensor.

2.9. Electrochemical measurement of MCF-7 cells

MCF-7 cells detection was carried out in the sandwich assay format. The resulting electrochemical biosensor was incubated with various concentrations of MCF-7 cells for 1 h at 37 °C, and then immersed in 6 μL of the prepared SP solution for another 1 h. After that, the electrode was washed with PBS to remove

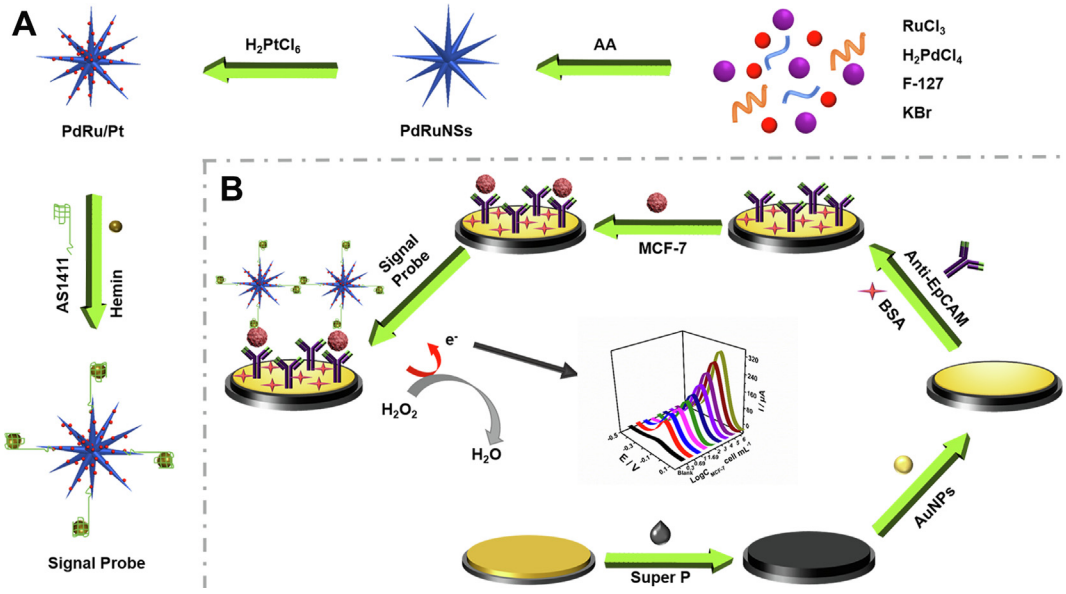

Scheme 1. Schematic illustration of the fabricating of the hemin/G-quadruplex labelled PdRu/Pt heterostructure (A) and electrochemical biosensor for CTCs (MCF-7 cell as a model) detection (B).

unbound signal conjugates and readied for performing the electrochemical analysis.

2.10. Cell culture and separation

Human breast cancer cell line (MCF-7 cells), human embryonic kidney cell line (HEK 293T cells) and human cervical cancer cell line (HeLa cells) were cultured in Dulbecco's Modified Eagle Medium (DMEM) replenished with 10% fetal bovine serum (FBS) and 1% penicillin–streptomycin, then all cells were put into cell incubator (humidified at 37 °C, 5% CO_2). The supernatant of cell culture was discarded, and the cells were routinely digested with 0.25% trypsin for 1–2 min after washing with 0.01 M PBS. Subsequently, the digested free cells were collected, centrifuged 500 rpm for 10 min and replanted in the fresh growth medium.

The cells were separated from the spent medium by centrifugation at 500 rpm for 10 min, rinsed twice and resuspended in PBS buffer. The concentration of cells was counted using a Neubauer Improved Hemocytometer. Afterwards, the cell suspension was diluted to a certain concentration by PBS.

3. Results and discussion

3.1. Characterization of the materials

3.1.1. Morphological characterization of Super P and AuNPs

Field emission scanning electron microscopy (FE-SEM) and transmission electron microscopy (TEM) were used to characterize the morphology of Super P and AuNPs, respectively. Fig. S2A showed the spherically shaped structure of Super P with size approximately of 60–80 nm and uniformly dispersed after ultrasound treatment. Such morphology endows the carbon black material a large specific surface area, which promises Super P the potential to provide conductive junction points sufficiently and improve electrical conductivity [23]. Fig. S2B showed that, the synthetic AuNPs had good performance of homogeneous dispersion with diameter size on average of 15 nm.

3.1.2. Characterization of the PdRuNSs and PdRu/Pt

The structures and morphologies of the PdRuNSs and PdRu/Pt were investigated using of TEM and SEM. As depicted in Fig. 1A, the different magnification TEM images of PdRuNSs suggested a branch-like structure and an average particle size of about 166 nm (Fig. S1C). Furthermore, PtNPs were noticeable found on the PdRuNSs surface with relatively heterogenous size distribution (Fig. 1B), which indicated that Pt precursors were sufficiently reduced in synthesis process. The 3D branch-like morphology of PdRuNSs and PdRu/Pt were confirmed by SEM images (Fig. S3A–B). What's more, when PtNPs decorated on PdRuNSs surface, the nano-spines structure further grew uniformly along all the directions, with an average length and width around 130 nm and 10 nm, respectively. This phenomenon of hyperbranched growth might be due to the second continual heat treatment at 95 °C and the reductants addition led to further growth of the nanocrystalline branches [26,27]. Hyperbranched PdRuNSs would serve as better molecular carrier to load more PtNPs and nucleic acid probes than PdRuNSs. In addition, the TEM and EDS results in Fig. S4 reveal that PdNCs were synthesized with homogeneous dispersion around 26 nm. The morphology change might be due to the absence of Ru element coordination [28].

As depicted by the high-resolution TEM (HRTEM) images (Fig. 1C–D), a plenty of clear lattice fringes can be observed. The lattice spacing distances were approximately 0.223 and 0.227 nm, which were well assigned to the typical {1 1 1} facets of face-centered cubic (fcc) PdRu alloy, indicating the incorporation

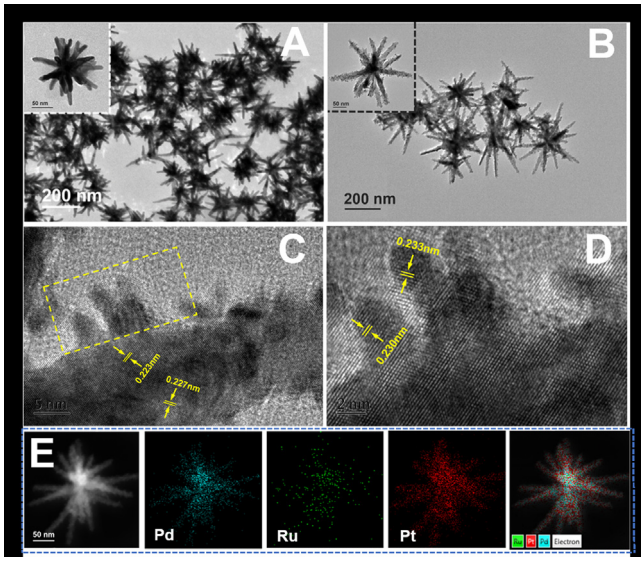

Fig. 1. TEM images of PdRuNSs (A) and PdRu/Pt (B). High-resolution TEM image (D) taken from the marked section in (C). The elemental mapping of PdRu/Pt (E). Insets in A and B are the high-magnification of PdRuNSs and PdRu/Pt, respectively.

of Ru atoms into the Pd lattice [28]. Meanwhile, the lattice fringes with an interplanar spacing of 0.230 and 0.233 nm were also emerged from the marked regions, good corresponding to the {1 1 1} crystal plane of the Pt fcc structure [29]. The lattice fringes coherently extended from the body of PdRuNSs to the PtNPs, signifying the epitaxial decorated of PtNPs with high degree of crystallinity. These observations showed PdRu/Pt heterostructures had a quite rough surface after the reduction of platinum particles, which would provide high-density of exposed active sites for catalytic reactions and then significantly promote the electron transfer rates.

The structure and elemental distribution of PdRu/Pt were strongly certificated via HAADF-STEM energy dispersive X-ray (EDX) elemental mapping. As Fig. 1E, the Pd and Ru elements were mainly distributed in the inner section, which confirmed the homogeneous alloyed nature of PdRuNSs. Remarkably, the Pt elements were evenly distributed around the perimeter, revealing the formation of PdRu/Pt hierarchical structures. Also, the atomic ratio of Pd, Ru and Pt were estimated approximately to be 83.31:1.09:15.60 by the energy-dispersive X-ray spectroscopy (EDS) spectrum (Fig. 2A), which was further unveiled by the analysis of the line scanning profiles (Fig. 2B). Both TEM and elemental analysis results confirmed the PtNPs were evenly dispersed over the entire surface of the PdRuNSs. On account of the strong surface energy, Pt tended to form stable structures such as particles or island on the core substrates, which might in possession of more durability in applications [30].

X-ray diffraction (XRD) pattern was conducted to investigate the crystalline structure of PdRu/Pt, using standard Pd (JCPDS-46-1043), Ru (JCPDS-88-2333) and Pt (JCPDS-40-0802) as the references. As Fig. 2C distinctly showed, there exhibited four characteristic peaks at around 40.17°, 46.58°, 67.97° and 82.06°, which were greatly consisted with the (1 1 1), (2 0 0), (2 2 0) and (3 1 1) facets of the fcc structure, respectively, indicating the polycrystalline character of the integrated PdRu/Pt [31]. It is noteworthy that the peaks of PdRu/Pt were slightly shifted comparing with pure mono-metallic Pd, Ru and Pt, suggesting the lattice distance was changed during the formation of the polycrystalline structure for PdRu/Pt.

The chemical valence state and composition were further illuminated by X-ray photoelectron spectroscopy (XPS). Notably, there

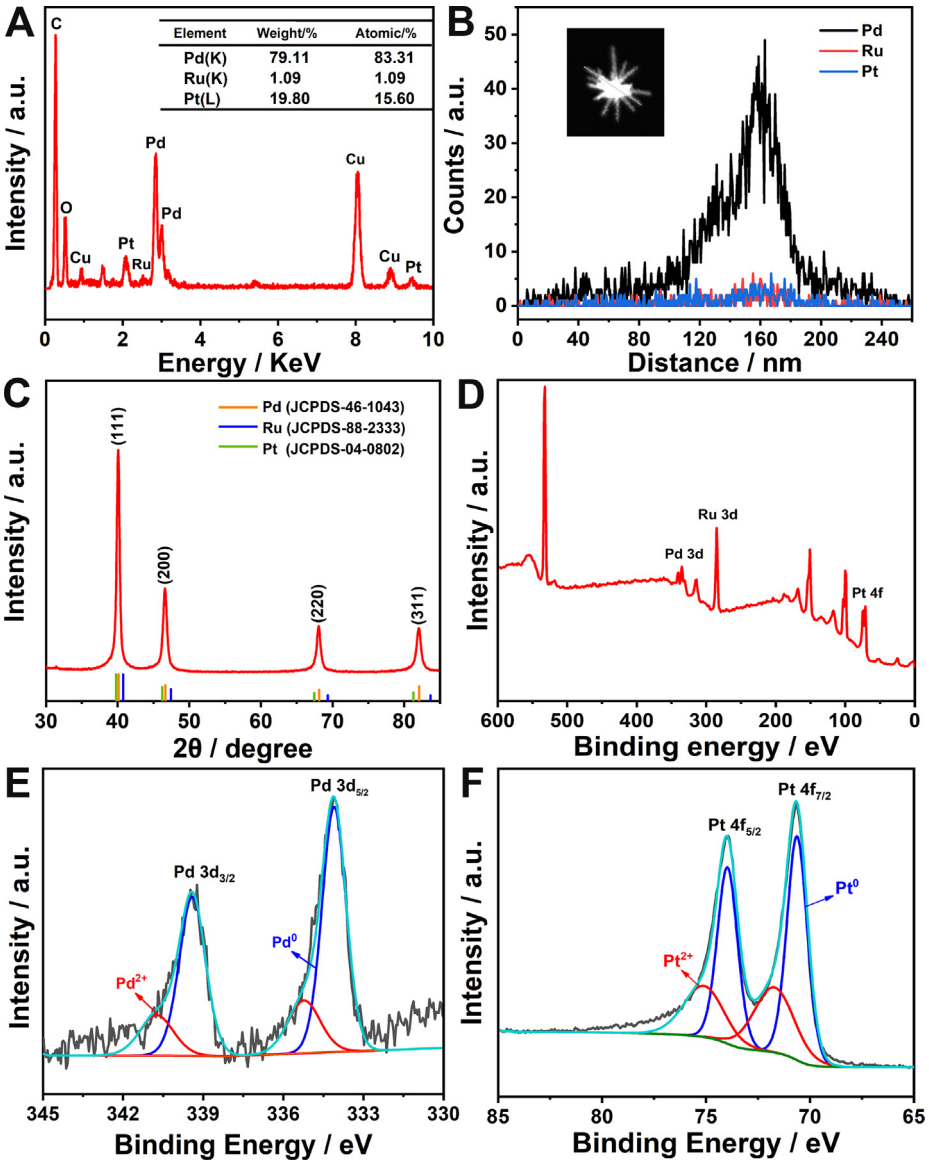

Fig. 2. The EDS spectrum (A), and line scanning profiles (B) of PdRu/Pt. (C) XRD spectrum of PdRu/Pt. The standard XRD spectra of pure Pd (JCPDS-46-1043), Ru (JCPDS-88-2333) and Pt (JCPDS-04-0802) are provided for comparison. Survey (D), high-resolution Pd 3d (E) and Pt 4f (F) XPS spectra of PdRu/Pt. Insets in A and B display the weight and atomic ratios of Pd, Ru and Pt, and HAADF-STEM image, respectively.

were Pd, Ru and Pt elements identified in the survey XPS spectrum of the PdRu/Pt (Fig. 2D). The high-resolution Pd 3d XPS spectrum showed two doublets of peaks (Fig. 2E) located at 340.78 (3d 3/2) and 335.21 (3d 5/2) eV; 339.40 (3d3/2) and 334.09 (3d5/2) eV, which are the characteristics of those Pd^{2+} and Pd^0 species, respectively [32]. This result confirmed that palladium ions were manly reserved in the form of Pd^0 in the heterostructures. Besides, the peak of Ru^0 was located at 283.29 (3d3/2) eV (Fig. S5A), revealed the presence of Ru in the products [33]. Furthermore, there were no obvious peaks observed in the high-resolution Ru 3p region (Fig. S5B) due to limited Ru loading. This result was in good accordance with the EDS analyses.

Meanwhile, as shown in the high-resolution XPS segment of Pt 4f (Fig. 2F), the stronger couple for 4f 7/2 (70.62 eV) and 4f 5/2 (73.95 eV) was the well assigned to metallic Pt^0. Nevertheless, while the weaker pair for 4f 7/2 (71.73 eV) and 4f 5/2 (75.15 eV) was attributed to Pt^{2+} species [34]. This result confirmed that the $PtCl_6^{2+}$ was effectively reduced to metallic Pt in the products. More importantly, those phenomena suggested that metallic Pt^0 and Pd^0 species are the prominent in the PdRu/Pt, illuminating the efficient reduction of the two metal precursors in the synthetic processes. Above-mentioned findings jointly demonstrated that the PdRu/Pt heterostructures were synthesized successfully.

In general, the formation mechanism of the PdRu/Pt was investigated shortly. At the original phases, the two metal precursors (H_2PdCl_4 and $RuCl_3$) were concurrently reduced to Pd and Ru atoms in the presence of ascorbic acid. In the meantime, the freshly-shaped metal atoms were immediately fused together to yield PdRu nuclei, which the decrement the surface free energy and improvement of dispersity in solution can be achieved [35]. As the reaction proceeded, the PdRu alloyed nucleis were gradually evolved into RuPdNSs via the guidance of F127, slow orientation and epitaxial-growth by Ostwald ripening process with the reaction time gradually prolonging [36]. In addition, under the existences of AA and elevated temperatures, PtNPs were uniformly embellished on the surface of PdRuNSs after thoroughly utilizing

of the Pt precursor. At the same time, PdRuNSs were further grew uniformly in all directions, ultimately formed hyperbranched PdRu/Pt heterogeneous structure.

As a nonionic surfactants, F127 can induce the combination of bromide ions and dioxygen to achieve the branch-like structure dispersion independently and catalytic activity [37]. We applied F127 as a growth-directing agent and capping agent to tune the morphology of the PdRu/Pt products. In the controlled experiments, inadequacy (15 g) or excess (45 g) F127 even formed severe aggregation of PdRu/Pt (Fig. S6). It demonstrated the meaningful impact of the proper F127 content in the synthesis process.

3.2. Characterization of stepwise fabrication of the electrochemical biosensor

To investigate the interfacial characteristics of the electrodes, CV and EIS measure methods were generally used to measure the sensing interface after each modified step. The CV curves of different fabricated step on electrodes were illustrated in Fig. 3A. After Super P (curve b) and AuNPs (curve c) immobilization onto the electrode, the peak currents visibly increased comparing with the bare gold electrode (curve a). Those signal changes should be ascribed to good electrical conductivity and large specific surface area of Super P and AuNPs. Moreover, the combination of these two nanomaterials ideally improves the sensitivity of biosensors. As expected, when the electrode was further modified with the antibody possesses of amino group owing to the Au-NH_2 bond, a decreased peak current was observed (curve d) due to steric hindrance of antibody. The peak current decreased further when the nonspecific sites were blocked by non-conductive BSA (curve e). After the immobilization of MCF-7 cells (curve f), the peak current was decreased similarly. It signified the formation of the nonconductive immune complexes which prevented the electron migration from cells to electrodes. These results demonstrated the biosensor was constructed successfully.

Subsequently, EIS was also used to assess the interface properties of electrode during the stepwise modification procedures. Each of the EIS Nyquist plots comprises of a semicircle curve portion and a straight-line portion, corresponding to the interfacial charge-transfer resistance (Rct) and electron diffusion, respectively. As displayed in Fig. 3B, after modified the Super P (curve b) and AuNPs (curve c) on the gold electrode in succession, the Rct values were decreased significantly, owing to the excellent conductivity of Super P and Au NPs that can expedite the electron transport process. However, when the antibody (curve d) and BSA (curve e) were immobilized onto the modified electrode surface step by step, the Ret values increased successively. After MCF-7 cells (curve f) were specifically captured by anti-EpCAM antibody attached onto the gold electrode, the Rct grows as expected due to hinderance of electron transfer by immobilized nonconductive material. The EIS results were in greatly accordance with the previous CV data, indicative of the feasible of the presented biosensor. Additionally, atomic force microscopy (AFM) was serviced to morphologically characterize the modification process of electrode (Fig. S7), further verified the well-organized modified process of this biosensor. A detailed description was provided in the SI.

Moreover, fluorescence microscopy analysis was utilized to test the specificity of RP towards MCF-7 cell (Fig. S8). Specifically, MCF-7 cells and HEK 293T cells (as negative control cells) were incubated with FAM-modified aptamers (FAM-RPs), respectively. Remarkable green fluorescence signal was exhibited on the group of MCF-7 cells incubated with FAM-RPs. This implied that the RP can bind to MCF-7 specifically.

In addition, the voltammetry was used to monitor the ability of stepwise fabrication on catalytic reduction of H_2O_2. As shown in Fig. 3C, an immensely strong DPV response only could be measured in the presence of MCF-7 cells. Nevertheless, no obvious DPV signals were observed without MCF-7 cells. Therefore, the based-nanomaterials sandwich-type electrochemistry biosensor was applicable for MCF-7 cells detection.

3.3. Comparison of different signal amplification strategies

To verify the signal amplification effect of the proposed biosensor, four groups of comparative experiments were prepared to detect the same cells concentration in optimized condition. The four groups included four signal labels (a) PdNCs-RP-BSA; (b) PdRuNSs-RP-BSA; (c) PdRu/Pt-RP-BSA and (d) PdRu/Pt-hemin/G4-BSA and two typed of electrode modification (e) bare Au electrode and (f) Au electrode with Super P/AuNPs. As shown in Fig. 4A, when the PdRuNSs-RP-BSA was selected as the signal labels to detect target cells, the biosensor exhibited a much higher current response than in the case of PdNCs-RP-BSA. This result illuminated the catalytic peroxidation ability of PdRuNSs was improved effectively due to the synergistic reaction of bimetals. Additionally, a sharply increase showed in current response when the biosensor was incubated with PdRu/Pt-RP-BSA compared to PdRuNSs-RP-BSA, which was attributed to uniform modification of PtNPs and the formed heterogeneous structure of the nanomaterial that enhance the catalytic effect on H_2O_2 to increase the electrochemical response (Fig. 4B). Meanwhile, the catalytic properties of different metal components (PdNCs, PdRuNSs and PdRu/Pt) were compared by DPV curves in same concentration. Fig. S9 showed that PdRu/Pt represented the best outstanding catalytic performance. These results might due to the heterogeneous structure of PdRu/Pt within explicit multi-metallic interface [30]. The detailed experimental steps have been specified in SI. When the biosensor was incubated with SP, the peak current further

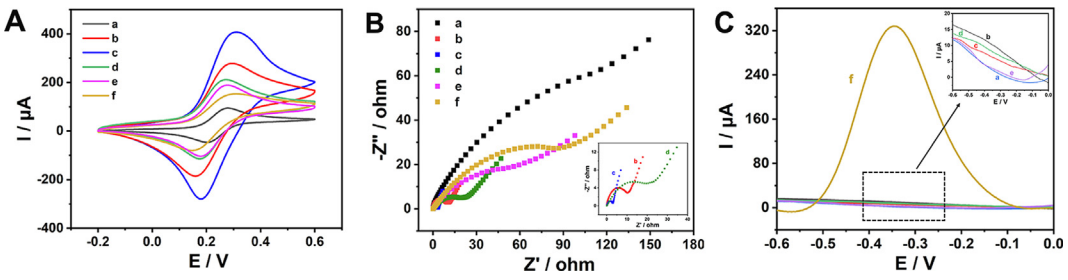

Fig. 3. CV (A) and EIS (B) of (a) bare gold electrode, (b) Super P/gold electrode, (c) AuNPs/Super P/gold electrode, (d) antibody/AuNPs/Super P/gold electrode, (e) BSA/antibody/AuNPs/Super P/gold electrode, and (f) MCF-7 cells/BSA/antibody/AuNPs/Super P/gold electrode obtained in 0.1 M KCl containing 5 mM $[Fe(CN)_6]^{3-/4-}$. The DPV current responses (C) of (a) Super P/gold electrode, (b) AuNPs/Super P/gold electrode, (c) Antibody/AuNPs/Super P/gold electrode, (d) BSA/antibody/AuNPs/Super P/gold electrode, (e) MCF-7 cells/BSA/antibody/AuNPs/Super P/gold electrode and (f) SP/MCF-7 cells/BSA/antibody/AuNPs/Super P/gold electrode measured in pH 6.0 PBS (100 mM, 25 mL) containing 20 mM H_2O_2.

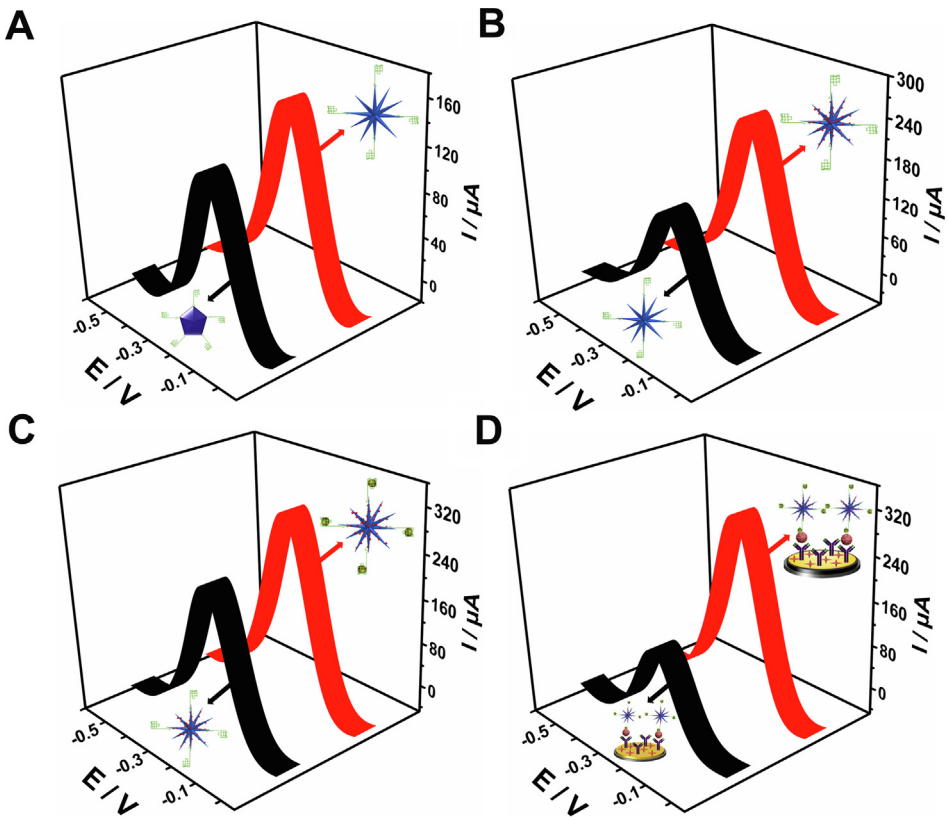

Fig. 4. The DPV signal of the as-built electrochemical biosensor incubated with different nanomaterials: (A) signal material: PdNCs-RP-BSA (blank line) and PdRuNSs-RP-BSA (red line); (B) signal material: PdRuNSs-RP-BSA (blank line) and PdRu/Pt-RP-BSA (red line); (C) signal material: PdRu/Pt-RP-BSA (blank line) and hemin/G4 labelled PdRu/Pt (red line); (D) substrate material: bare gold electrode (blank line) and Au electrode with Super P/AuNPs (red line). (For interpretation of the references to color in this figure legend, the reader is referred to the web version of this article.)

increased (Fig. 4C), partially for the reason that the co-catalysis ability of PdRu/Pt and hemin/G4 DNAzyme toward hydrogen peroxide. Notably, the change of DPV signal by Super P/AuNPs modified Au electrode was much bigger than that of bare Au electrode (Fig. 4D). This is probably linked to the enhancement of large specific surface area and the improvement of electrical conductivity by used of Super P/AuNPs. Thus, the proposed multiple signal amplification strategy (Super P/AuNPs and hemin/G4 labelled PdRu/Pt) was validated effectively and it was beneficial to construct the biosensor with high sensitivity.

3.4. Optimization of the analytical conditions

To optimize the experimental conditions, the pH of PBS, the proportion of PdRu/Pt and aptamer, the incubation time and concentration of antibody for the antibody-target cell reaction, the binding time of SP to target cell MCF-7, and the blocking time of BSA were optimized successively. All optimization experiments were performed by using DPV assay at MCF-7 concentration of 10^6 cells mL^{-1}.

In biosensing platform, the pH in the buffer solution had great influences on the bioreactivity and stability of the immobilized biomolecules. Hence, the pH may impact the analytical performance of the current device. When the pH was adjusted from 4 to 7, the corresponding DPV curves peaks gradually increased and reached a maximum at 6. At pH > 6, the electrochemcial response signal drops sharply (Fig. S10A). Thereby pH = 6 is selected in the subsequent experiments.

Hemin/G4 labelled PdRu/Pt, as the signal amplification probe, was a crucial factor in the process of measurement. Different proportion of PdRu/Pt and aptamer may exert an enormous impact on the catalytic performance for the reduction of H_2O_2. As shown in Fig S10B, the current signals were increased with the growing proportions from 50:1 to 50:2, then decreased when the proportions were 50:2.5 and 50:3. Therefore, 50:2 was chosen as the optimal proportion of PdRu/Pt and aptamer. Furthermore, the voltammetry response of different incubation times of SP towards MCF-7 cell ranging from 30 to 70 min was investigated (Fig. S10C). The DPV responses were increased since the incubation time in range of 20–50 min and reached a maximum at 60 min. Further increase of incubation time did not improve the current any more, indicative of the equilibrium of reaction of cell and SP. Therefore, the highest peak current was received when the incubation time of SP and MCF-7 cell was 60 min.

Since the concentration of anti-EpCAM antibody directly determined the binding efficiency of cells, it was necessary to be optimized. Fig. S10D showed the peak currents consecutively increase with growing concentration of antibody from 20 μg mL^{-1} to 70 μg mL^{-1}, and then with the upon increasing of the concentration, the DPV response declined. As a result, 70 μg mL^{-1} was selected as the optimal concentration of anti-EpCAM antibody against MCF-7 cells.

The incubation time of antibody and MCF-7 cell also had a large influence of measurement results and was tested in the range from 20 to 70 min (Fig. S10E). Distinctly, the peak currents successively increased by prolonging the incubation time, achieving the maximum at 60 min, and then inclining to be stable by further extending the time over 60 min. Therefore, 60 min was the best for measurement of MCF-7 cells in the study.

In Fig S10F, accompanying the increased of the blocking time, the electrochemical signals decreased rapidly and remained steady at approximately 50 min. This result indicated that the nonspecific

site of modified electrode had been largely hindered. At the meantime, the background signal of analysis was also reduced. Therefore, 50 min was chosen as the optimal blocking time for BSA.

3.5. Analytical performance of the proposed electrochemical biosensor

Under the optimal conditions, MCF-7 cells with different concentrations were detected by used of SP and Super P/AuNPs to characterize the detection sensitivity of this proposed biosensor. As Fig. 5A shows, the DPV current responses gradually enhanced corresponding with increasing concentrations of target cells from 2 cells mL^{-1} to 1 × 10^6 cells mL^{-1}. Moreover, the calibration plot depicted a good linear relationship between the DPV values and logarithm values of MCF-7 cells (Fig. 5B). The fitted linear regression equation is construed as follows: I (μA) = 87.763 + 38.491log$C_{(MCF\text{-}7)}$ (cells mL^{-1}), with a correlation coefficient of R^2 = 0.998 and LOD down to 2 cells mL^{-1} (S/N = 3). The extremely low detection limit, detected by multiple signal amplification biosensor, might be attributed to following factors: firstly, Super P and AuNPs, which modified on electrode, have favorable electron conductivity and abundant surface binding sites; secondly, the PdRu/Pt heterostructures have prominent catalytic activity for H_2O_2; finally, hemin/G4 mimics peroxidase further enhances the catalytic ability for H_2O_2 to increase the sensitivity of the biosensor significantly. Moreover, a comparison with the recent method regarding the detection of CTC is shown in Table S1. The comparison clearly showed the as-constructed electrochemical biosensor had preeminent or comparable detection sensitivity. Therefore, the as-built biosensor achieved distinguished performance to sensitive detection of MCF-7 cells.

3.6. Reproducibility, specificity and stability

The reproducibility of the biosensor was also investigated by recording the current response. By detecting the same concentration of MCF-7 (10^6 cells $mL^{-1)}$ under the optimized conditions in six biosensors assembled independently, the relative standard deviation (RSD) of the intra-assay and inter-assay of the biosensor were approximately 2.08% and 2.32% (Fig. 5C). This result revealed the satisfactory reproducibility of the proposed electrochemical biosensor.

As a proposed new method for detecting tumor cells, the specificity is a vital parameter for evaluating the performances of biosensor [38]. To assess the specificity, several 1 × 10^6 cells mL^{-1} nontarget interfering cell lines including Hela cells (EpCAM-negative), HEK 293T cells (AS1411-negative), white blood cells (WBCs) and red blood cells (RBCs) were tested. As Fig. 5D shown, compared with blank, no apparent current signals were generated toward 1 × 10^6 cell mL^{-1} of other non-target ones. However, the current response of MCF-7 cells with the same concentration was conspicuous highly and almost the same with the mixtures, manifesting that the biosensor had high specificity and potential in practical applications.

The stability of the biosensor was also investigated by a differential pulse voltammetry in the presence of MCF-7 cells (10^6-cells mL^{-1}). The fabricated biosensors were stored at 4 °C few days before use. As can be seen in Table S2, after being kept in a refrigerator for 7 days, 98.1% of its initial current response was retained compared with that of a freshly modified electrode. After 21 days, the current response retained 87.9% of their initial ones, which signified the favorable stability of the established biosensor.

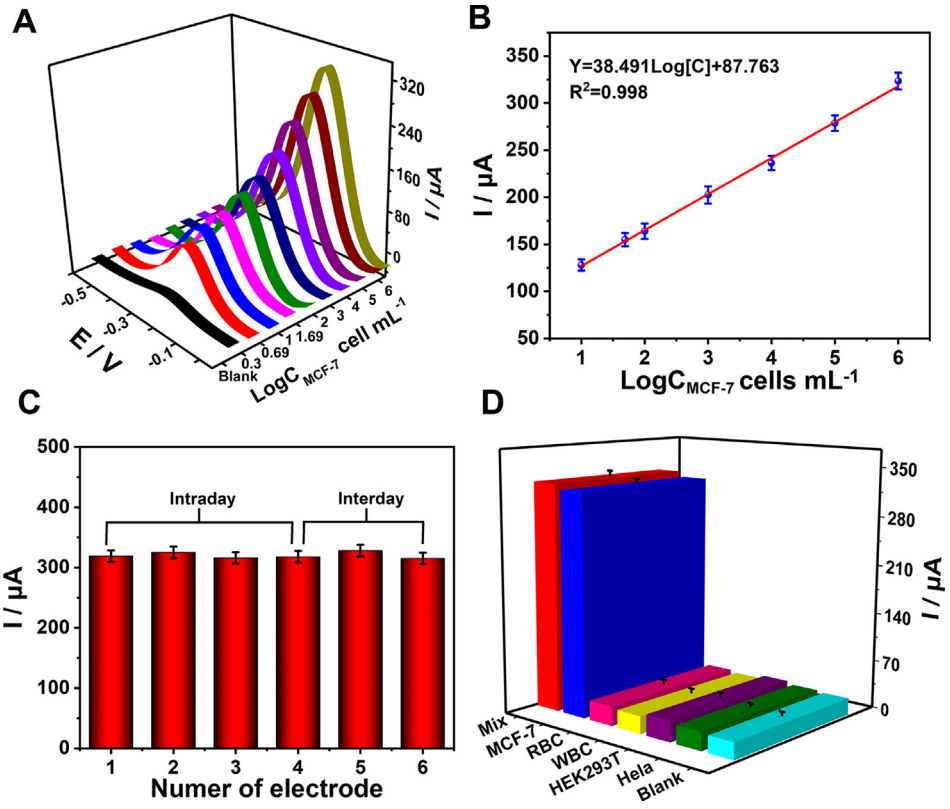

Fig. 5. (A) DPV curves for the proposed biosensor with 2, 5, 10, 50, 10^2, 10^3, 10^4, 10^5, 10^6 cells mL^{-1} of MCF-7 cells. (B) Calibration plot of the biosensor for different concentrations of MCF-7 cells from 10 to 10^6 cells mL^{-1}. (C) Reproducibility of 6 different electrodes modified with 10^6 cells mL^{-1}. (D) Specificity of the biosensor investigated with blank control, HeLa cells, HEK 293T cells, WBCs and RBCs and the related mixture. Error bars = SD (n = 5).

3.7. Application for the analysis of serum samples

To validate the practical availability and accuracy of the present electrochemical biosensor, several concentrations of MCF-7 (10, 10^2, 10^3, 10^4 were added to the human blood samples (obtained from the Chongqing University Central Hospital). Then the current responses of these blood samples using the proposed biosensor were recorded. As seen in Table S3, the recovery rates were calculated as 97.8–101.25% with RSD ranging from 2.05% to 2.80%. These results implied that the present electrochemical method had good capability of combating multiple interference and effective recognition of tumor cells in practical blood samples with good accuracy. In general, the proposed biosensor had the potential applications to quantified detection of MCF-7 cells in clinical practice analyses.

4. Conclusion

To sum up, we reported a new PdRu/Pt hierarchical composite synthesized via hydrothermal reaction and integrated with hemin/G-quadruplex to serve as signal amplification probe to construct a sandwich-type electrochemical biosensor. Morphological features, elemental distribution, crystalline structure and valence state were analyzed to characterize as-synthesized PdRu/Pt [31,32,34]. In the hybrid composite, PdRu alloyed nuclei were evolved into RuPdNSs under the guidance of F127 and slow Ostwald ripening process whereas PtNPs were uniformly decorated on the surface of PdRuNSs via ascorbic acid-assisted reduction [35,36]. Higher catalytic activity was observed compared with PdRuPt alloy likely due to rational structural design and explicit multi-metallic interface [24]. What's more, hemin/G4 DNAzyme was used to amplify electrochemical current signal and improve specificity [20]. After integration with hemin/G-quadruplex, as-constructed biosensor showed good sensitivity towards CTCs down to 2 cells mL^{-1} in resuspension solution. We envision our preliminary work will not only introduce a new nanomaterials synthesis to construct electrochemical biosensors, but also alternate a useful strategy to improve sensitivity for rare CTCs detection in blood samples.

CRediT authorship contribution statement

Xi Zhou: Conceptualization, Methodology, Writing - original draft. **Qinli Pu:** Writing - review & editing, Investigation. **Hongyan Yu:** Data curation, Software. **Yang Peng:** Investigation, Software. **Junjie Li:** Writing - review & editing, Data curation. **Yujun Yang:** Software, Validation. **Huajian Chen:** Validation. **Yaguang Weng:** Conceptualization, Supervision, Project administration. **Guoming Xie:** Funding acquisition, Conceptualization, Project administration, Supervision, Writing - review & editing.

Declaration of Competing Interest

The authors declare that they have no known competing financial interests or personal relationships that could have appeared to influence the work reported in this paper.

Acknowledgments

This work was financially supported by the Natural Science Research Foundation of China (81702101) and the Graduate Scientific Research and Innovation Project of Chongqing (CYB19162).

Appendix A. Supplementary material

Supplementary data to this article can be found online at https://doi.org/10.1016/j.jcis.2021.05.006.

References

[1] K. Pantel, M.R. Speicher, The biology of circulating tumor cells, Oncogene 35 (2015) 1216–1244.
[2] S. Chen, A. El-Heliebi, G. Tauber, T. Langsenlehner, M. Pötscher, K. Kashofer, Z. Czyż, B. Polzer, S. Riethdorf, A. Kuske, G. Leitinger, K. Pantel, T. Kroneis, P. Sedlmayr, Catch and Release: rare cell analysis from a functionalised medical wire, Sci. Rep. 7 (2017) 43424.
[3] B. Hong, Y. Zu, Detecting circulating tumor cells: current challenges and new trends, Theranostics 3 (6) (2013) 377–394.
[4] P. Economopoulou, I. Kotsantis, E. Kyrodimos, E. Lianidou, A. Psyrri, Liquid biopsy: An emerging prognostic and predictive tool in Head and Neck Squamous Cell Carcinoma (HNSCC). Focus on Circulating Tumor Cells (CTCs), Oral Oncol. 74 (2017) 83–89.
[5] Z. Shen, A. Wu, X. Chen, Current detection technologies for circulating tumor cells, Chem. Soc. Rev. 46 (8) (2017) 2038–2056.
[6] A. Majewski, U. Stahlschmidt, V. Jérôme, R. Freitag, A. Müller, H. Schmalz, PDMAEMA-grafted core-shell-corona particles for nonviral gene delivery and magnetic cell separation, Biomacromolecules 14 (9) (2013) 3081–3090.
[7] J. Swennenhuis, G. van Dalum, L. Zeune, L. Terstappen, Improving the Cell Search® system, Expert Rev. Mol. Diagn. 16 (12) (2016) 1291–1305.
[8] L. Wang, Y. Li, J. Xu, A. Zhang, X. Wang, R. Tang, X. Zhang, H. Yin, M. Liu, D. Wang, P. Lin, L. Shen, J. Dong, Quantified postsurgical small cell size CTCs and EpCAM circulating tumor stem cells with cytogenetic abnormalities in hepatocellular carcinoma patients determine cancer relapse, Cancer Lett. 412 (2018) 99–107.
[9] Z. Shen, A. Wu, X. Chen, Current Detection Technologies of Circulating Tumor Cells, Chem. Soc. Rev. 46 (8) (2017) 2038–2056.
[10] Y. Wei, X. Liu, C. Mao, H. Niu, J. Song, B. Jin, Highly sensitive electrochemical biosensor for streptavidin detection based on CdSe quantum dots, Biosens. Bioelectron. 103 (30) (2018) 99–103.
[11] Y. Kuo, C. Lee, C. Lin, Improving sensitivity of a miniaturized label-free electrochemical biosensor using zigzag electrodes, Biosens. Bioelectron. 103 (2018) 130–137.
[12] P. Scrimin, L. Prins, Sensing through signal amplification, Chem. Soc. Rev. 40 (9) (2011) 4488–4505.
[13] X. Fu, J. He, C. Zhang, J. Chen, Y. Wen, J. Li, W. Mao, H. Zhong, J. Wu, X. Ji, C. Yu, bioelectronics, Trimetallic signal amplification aptasensor for TSP-1 detection based on Ce-MOF@Au and AuPtRu nanocomposites, Biosens. Bioelectron. 132 (2019) 302–309.
[14] S. Lv, K. Zhang, L. Zhu, D. Tang, D. Knopp, H2-based electrochemical biosensor with Pd nanowires@ZIF-67 molecular sieve bilayered sensing interface for immunoassay, Anal. Chem. 91 (18) (2019) 12055–12062.
[15] Z. Wu, S. Shan, S. Zang, C. Zhong, Dynamic core-shell and alloy structures of multimetallic nanomaterials and their catalytic synergies, Acc. Chem. Res. 53 (12) (2020) 2913–2924.
[16] M. Axet, K. Philippot, Catalysis with colloidal ruthenium nanoparticles, Chem. Rev. 120 (2) (2020) 1085–1145.
[17] X. Huo, X. Liu, J. Liu, P. Sukumaran, S. Alwarappan, D.K. Wong, Strategic applications of nanomaterials as sensing platforms and signal amplification markers at electrochemical immunosensors, Electroanalysis 28 (2016) 1–21.
[18] M. Gotrik, T. Feagin, A. Csordas, M. Nakamoto, H. Soh, Advancements in aptamer discovery technologies, Chem. Res. 49 (9) (2016) 1903–1910.
[19] G. Collie, G. Parkinson, The application of DNA and RNA G-quadruplexes to therapeutic medicines, Chem. Soc. Rev. 40 (12) (2011) 5867–5892.
[20] S. Chen, P. Liu, K. Su, X. Li, Z. Qin, W. Xu, J. Chen, C. Li, J. Qiu, Electrochemical aptasensor for thrombin using co-catalysis of hemin/G-quadruplex DNAzyme and octahedral Cu2O-Au nanocomposites for signal amplification, Biosens. Bioelectron. 99 (2018) 338–345.
[21] S. Tang, H. Shen, Y. Hao, Z. Huang, Y. Tao, Y. Peng, Y. Guo, G. Xie, W.J.B. Feng, bioelectronics, A novel cytosensor based on Pt@Ag nanoflowers and AuNPs/Acetylene black for ultrasensitive and highly specific detection of Circulating Tumor Cells, Biosens. Bioelectron. 104 (2018) 72–78.
[22] Y. Peng, Y. Peng, S. Tang, H. Shen, S. Sheng, Y. Wang, T. Wang, J. Cai, G. Xie, W. Feng, PdIrBP mesoporous nanospheres combined with superconductive carbon black for the electrochemical determination and collection of circulating tumor cells, Mikrochim. Acta 187 (4) (2020) 216.
[23] X. Zhang, G. Xie, D. Gou, P. Luo, Y. Yao, H. Chen, A novel enzyme-free electrochemical biosensor for rapid detection of Pseudomonas aeruginosa based on high catalytic Cu-ZrMOF and conductive Super P, Biosens. Bioelectron. 142 (2019) 111486.
[24] W. Mao, J. He, Z. Tang, C. Zhang, J. Chen, J. Li, C. Yu, A sensitive sandwich-type immunosensor for the detection of MCP-1 based on a rGO-TEPA-Thi-Au nanocomposite and novel RuPdPt trimetallic nanoalloy particles, Biosens. Bioelectron. 131 (2019) 67–73.
[25] Y. Gao, X. Deng, W. Wen, X. Zhang, S. Wang, Ultrasensitive paper based nucleic acid detection realized by three-dimensional DNA-AuNPs network amplification, Biosens. Bioelectron. 92 (2017) 529–535.

[26] V. Manikandan, A. Mirzaei, S. Vigneselvan, S. Kavita, J. Ch Andrasekaran, Role of ruthenium in the dielectric, magnetic properties of nickel ferrite (Ru–NiFe 2 O 4) nanoparticles and their application in hydrogen sensors, ACS Omega 4 (7) (2019) 12919–12926.
[27] S. Kunwar, P. Pandey, M. Sui, Q. Zhang, M.Y. Li, J. Lee, Effect of systematic control of Pd thickness and annealing temperature on the fabrication and evolution of palladium nanostructures on Si (111) via the solid state dewetting, Nanoscale Res. Lett. 12 (1) (2017) 364.
[28] W. Hongjing, L. Yinghao, L. Chunjie, W. Ziqiang, X. You, L. Xiaonian, X. Hairong, W. Liang, Hyperbranched PdRu nanospine assemblies: an efficient electrocatalyst for formic acid oxidation, J. Mater. Chem. A 6 (2018) -.
[29] K. Rui, G. Zhao, M. Lao, P. Cui, X. Zheng, X. Zheng, J. Zhu, W. Huang, S. Dou, W. Sun, Direct hybridization of noble metal nanostructures on 2D metal-organic framework nanosheets to catalyze hydrogen evolution, Nano. Lett. 19 (12) (2019) 8447–8453.
[30] T. Yang, G. Cao, Q. Huang, Y. Ma, S. Wan, H. Zhao, N. Li, X. Sun, F. Yin, Interfaces surface-limited synthesis of Pt nanocluster decorated Pd hierarchical structures with enhanced electrocatalytic activity toward oxygen reduction reaction, ACS Appl. Mater. Interfaces 7 (31) (2015) 17162–17170.
[31] J. Duan, X. Zheng, H. Niu, J. Feng, Q. Zhang, H. Huang, A. Wang, Porous dendritic PtRuPd nanospheres with enhanced catalytic activity and durability for ethylene glycol oxidation and oxygen reduction reactions, J. Colloid. Interface. Sci. 560 (2020) 467–474.
[32] M. Iqbal, Y. Kim, C. Li, B. Jiang, T. Takei, J. Lin, B. Yuliarto, Y. Bando, J. Henzie, Y. Yamauchi, Tailored design of mesoporous PdCu nanospheres with different compositions using polymeric micelles, ACS Appl. Mater. Interfaces 11 (40) (2019) 36544–36552.
[33] Z. Zhang, Y. Liu, B. Chen, Y. Gong, L. Gu, Z. Fan, N. Yang, Z. Lai, Y. Chen, J. Wang, Y. Huang, M. Sindoro, W. Niu, B. Li, Y. Zong, Y. Yang, X. Huang, F. Huo, W. Huang, H. Zhang, Submonolayered Ru deposited on ultrathin Pd nanosheets used for enhanced catalytic applications, Adv. Mater. 28 (46) (2016) 10282–10286.
[34] B. Yang, A.G. Agrios, Attachment of Pt nanoparticles to a metal oxide surface using a thiol-carboxyl bifunctional molecule, J. Colloid Interface Sci. 513 (2018) 464–469.
[35] B. Lim, Y. Xia, Metal nanocrystals with highly branched morphologies, Angew. Chem. Int. Ed. Engl. 50 (1) (2011) 76–85.
[36] F.Q. Shao, X.X. Lin, J.J. Feng, J. Yuan, J.R. Chen, A.J. Wang, Simple fabrication of core-shell AuPt@Pt nanocrystals supported on reduced graphene oxide for ethylene glycol oxidation and hydrogen evolution reactions, Electrochim. Acta 219 (2016) 321–329.
[37] S. Wang, G. Wu, X. Zhang, Z. Tian, N. Zhang, T. Hu, W. Dai, F. Qian, Stabilizing two IgG1 monoclonal antibodies by surfactants: Balance between aggregation prevention and structure perturbation, Eur. J. Pharm. Biopharm. 114 (2017) 263–277.
[38] Z. Luo, Q. Qi, L. Zhang, R. Zeng, L. Su, D. Tang, Branched polyethylenimine-modified upconversion nanohybrid-mediated photoelectrochemical immunoassay with synergistic effect of dual-purpose copper ions, Anal. Chem. 91 (2019) 4149–4156.